Journal Pre-proof

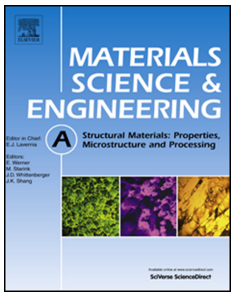

A new multi-component alloy with a nanostructured morphology and superior mechanical behavior

J.T. Fan, M.D. Zhang, L.J. Zhang, L.M. Fu, P.F. Yu, P.K. Liaw, G. Li

PII: S0921-5093(19)31402-9

DOI: https://doi.org/10.1016/j.msea.2019.138616

Reference: MSA 138616

To appear in: *Materials Science & Engineering A*

Received Date: 14 September 2019

Revised Date: 28 October 2019

Accepted Date: 30 October 2019

Please cite this article as: J.T. Fan, M.D. Zhang, L.J. Zhang, L.M. Fu, P.F. Yu, P.K. Liaw, G. Li, A new multi-component alloy with a nanostructured morphology and superior mechanical behavior, *Materials Science & Engineering A* (2019), doi: https://doi.org/10.1016/j.msea.2019.138616.

A new multi-component alloy with a nanostructured morphology and superior mechanical behavior

J.T. Fan[a, b†], M.D. Zhang[a†], L.J. Zhang[a†], L.M. Fu[b], P.F. Yu[a], P.K. Liaw[c], and G. Li[a,c*]

[a]State Key Laboratory of Metastable Materials Science and Technology, Yanshan University, Qinhuangdao 066004, China

[b]School of Materials Science and Engineering, Shanghai Jiao Tong University, Shanghai 200240, China

[c]Department of Materials Science and Engineering, The University of Tennessee, Knoxville, TN, 37996-2200, USA

[†]These authors contributed equally to the present work.

*Corresponding authors. *E-mail addresses*: gongli@ysu.edu.cn;

Abstract

Here, we develop a $Al_{13}Fe_{36}Co_{24}Ni_{24}C_3$ nanostructured alloy prepared via the arc-melting method. The newly-developed NS alloy consists of face-centered-cubic (FCC) and ordered-FCC ($L1_2$) dual-phase NS region and a small amount (~ 2.5 vol.%) of the ordered body-centered-cubic phase (B2). Significantly, the alloy exhibits outstanding harmony of the compressive yield strength (~ 1.5 GPa) and strain (~ 63%). The deformation substructure is mainly characterized by pronounced planar slip in the NS region. And the dynamic slip band refinement in the NS region coordinate with screw dislocations slip in the B2 grain enable the material shows excellent mechanical properties.

Keywords: Multi-component alloy; Coherent nanoparticles; Mechanical properties; Dynamic slip band refinement;

1. Introduction

Materials with nanoscale microstructures are usually associated with many great properties. For example, the metallic alloys with nanostructures exhibit high strength and hardness, strong fatigue resistance, and superior wear resistance [1-4]. Moreover, the biological materials (i.e. mollusk shells and sponge spicules) with natural nanostructures, display pleasant biological properties [5, 6]. As far as the present knowledge goes, several routes have been developed to fabricate nanostructured (NS) alloys, including electro-deposition, powder-metallurgy, dynamic

plastic deformation [7], and severe plastic deformation [8]. However, these aforementioned methods have two disadvantages, which will strongly limit their application in the industry. One is that the processes are complex and costly; another is that the sizes of NS samples prepared by these methods are limited [9]. For the applications of structural materials, generally, in addition to structural or properties, cost and ease of manufacturing are key features that must be considered. The development of a very efficient and low-cost method for achieving bulk NS alloys with outstanding mechanical properties is thus necessary.

In recent years, multi-component alloys (MCAs), also known as high-entropy alloys (HEAs), consisting of multi-principal elements in equi- or non-equiatomic percentages, have become a new research frontier in the materials community [10-12]. The MCAs have been seen as a promising candidate for engineering applications owing to their novel mechanical and functional properties, such as high-temperature structural stability [13], exceptional mechanical performance [14, 15], prominent fracture toughness at cryogenic temperatures [16] and, corrosion and fatigue resistance [17]. More specially, it was suggested that, depending on the compositions and processing conditions, there exists a strong tendency to yield bulk NS or ultrafine-microstructure (UFM) alloys in MCAs caused by the sluggish diffusion effect [9, 15, 17]. For instance, through tuning the composition in (FeCoNi)-AlTi complex alloy systems, Yang et al. [15] designed and prepared a novel $(FeCoNi)_{86}Al_7Ti_7$ alloy with the NS morphology and exceptional strength-ductility combination, in which the content of nanoparticles is more than 50 volume percent (vol. %). It is worth noting (however) that the as-cast $(FeCoNi)_{86}Al_7Ti_7$ alloy generally suffers from mechanical-working combined with the ensuing heat treatment, and ultimately achieved the bulk NS alloy complexly and costly. Although Lu et al. [9] have successfully prepared bulk $AlCoCr_xFeNi$ ($1.8 \leq x \leq 2.0$) ultrafine-microstructure HEAs via a low-cost and high efficient method, i.e., the direct solidification, the NS alloys were not obtained in the $AlCoCr_xFeNi$ HEAs system. Moreover, in our previous work [18] we have designed and fabricated an innovative dendrite-composite HEA ($Al_{18}Fe_{33.3}Co_{23}Ni_{23}C_{2.7}$) via direct solidification. Interestingly, it was found that

the interdendric (ID) region of the dendrite-composite HEA showed obvious an NS morphology.

In view of these pioneering studies, the present study was motivated by the question, whether it is possible to design and fabricate NS-MCAs with excellent mechanical properties through the direct solidification method. Our design concept aims to controllably increase the volume fraction of the NS-ID region for a novel NS-MCAs achieving by optimizing the composition of the dendrite-composite HEA [18]. Hence, a new multiphase $Al_{13}Fe_{36}Co_{24}Ni_{24}C_3$ MCA with an excellent NS morphology was successfully designed and fabricated. The newly-developed NS-MCA has exhibited superior mechanical behavior. We anticipate that the present study can provides the important insight for the future development of NS-MCAs for advanced structural applications.

2. Materials and methods

Alloy ingots with the composition of $Al_{13}Fe_{36}Co_{24}Ni_{24}C_3$ (atomic percent, at. %) were arc-melted in a vacuum hearth. The ingots were re-melted six times to improve the homogeneity ensued with suction casting (SC) into a water-cooled Cu mold to obtain cylindrical pillars with a diameter of 3 mm. To evaluate the material's mechanical properties, room-temperature uniaxial compression tests on the cylinder samples with a dimension of Φ3 mm × 6 mm were conducted at a constant strain rate of 5×10^{-4} s^{-1}. The detailed information of compression experiments can be seen in our previous work [18].

X-ray diffraction (XRD) was performed in the 2Theta range of 20° - 100° with a scanning speed of 4°/min to examine the crystal structure. The microstructures and chimerical compositions were characterized by a field-emission scanning electron microscope (SEM, Hitachi S-4800) and transmission electron microscopy (TEM) coupled with a selected area electron diffractometer (SAED) was performed on Talox-F200X operating under 200 kV. Electron backscattered diffraction (EBSD) characterizations were also performed using a Hitachi S-4800 SEM with the TSL OIM analysis software. The post-mortem TEM characterizations were further conducted to investigate the deformation microstructures of materials. The SEM

specimens were initially polished to 5000-grit SiC paper and, followed by mechanical polishing and, finally, the microstructures of alloys were revealed by etching in a weak solution of nitric acid and alcohol. The TEM samples were first mechanical grounding down to 30 μm thickness, and then using twin-jet polishing in a solution of 7% perchloric acid and 93% ethanol (vol. %) at around 20 ℃. Samples for EBSD examination were electro polished in a solution of 10% perchloric acid and 90% methanol at room temperature.

3. Results and discussion

Figure 1 shows the XRD pattern of the NS-MCA in the as-cast state. The typical peaks of a face-centered cubic (FCC) structure can be clearly observed. However, beyond that, the (110) peak of a body-centered-cubic (BCC) phase with the very faint intensity is also identified. The SEM and backscattered electron (BSE) images present microstructures of the NS-MCA, shown in Figure 2. As shown in Figure 2(a), the NS-MCA shows a typical equiaxed grain structure with second phase (dark regions) dispersed at grain boundaries and triple junctions of the matrix (light regions). Figure 2(b) provides a close-up view of the local microstructure within the matrix, interestingly, a considerable amount of near-spherical nanoparticles are uniformly dispersed in the matrix. A cautionary note is in order that there are no precipitates within the BCC phase. A recent study on $(FeCoNi)_{100-x-y}$-Al_xTi_y complex alloys also present the unique nanostructured morphology [15], while the difference is that our NS-MCA was achieved directly by the suction casting method without any mechanical working and heat treatment.

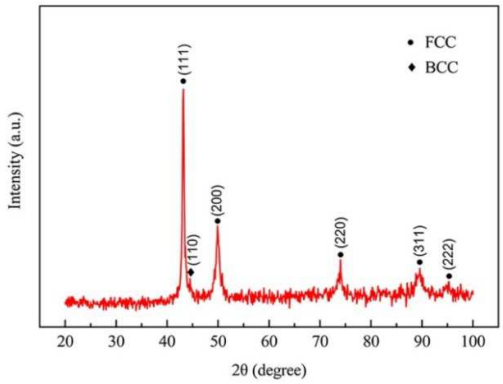

Fig. 1. XRD scattering and SEM/EBSD analysis of the $Al_{13}Fe_{36}Co_{24}Ni_{24}C_3$ NS-MCA.

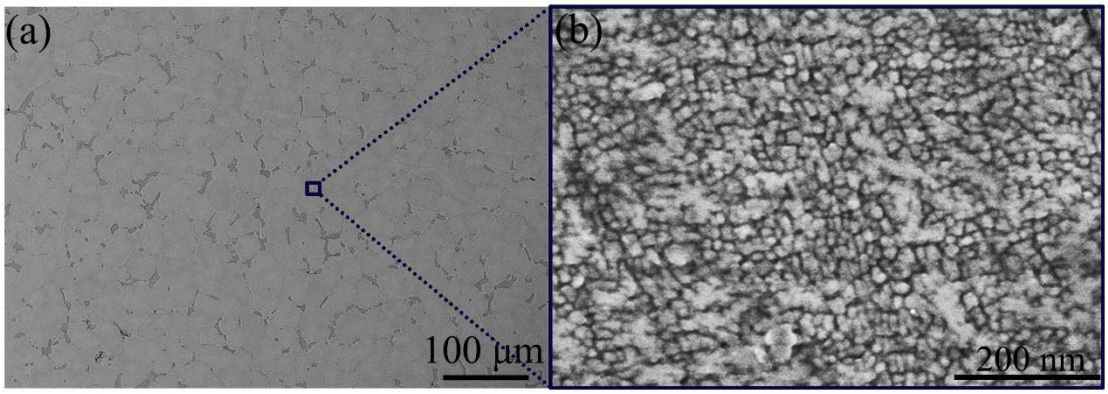

Fig. 2. The BSE-SEM image of the $Al_{13}Fe_{36}Co_{24}Ni_{24}C_3$ NS-MCA. (b) High magnification SEM image of the interior of the FCC grains, showing the nanostructured morphology.

To further study the microstructure of the NS-MCA, the EBSD analyses were performed on the sample. The typical EBSD inverse pole figure (IPF) map [Figure 3(a)] exhibits the equiaxed grains with inconsistent grain sizes varying from 10 to 70 μm. The EBSD phase map corresponding to the IPF map is presented in Figure 3(b), showing a small number (~ 2.5 vol. %) of the BCC phase (green) at FCC (light blue) grain boundaries and triple junctions, coinciding with the XRD and SEM results. The mean size of the BCC grains is ~ 8.2 μm, and the FCC grains have a mean size of ~ 33 μm, which is confirmed using the Image-J software [15] and, at least 100 grains are recorded. It is therefore visible that the volume fraction of the NS interdendritic region increases from 52 vol. % in the previous dendrite-composite HEA [18] to 97.5 vol. % in the current newly-developed NS-MCA [the matrix in Figures 2(a) and 3(b)]. Whereas, the dendritic region [the dark regions in Figure 2(a) and green regions in Figure 3(b)] shows a reverse trend, i.e. from 48 vol. % decreases to 2.5 vol. %. This chiefly is the reason owing to lower Al content in the present NS-MCA than in the dendrite-composite HEA since too high content of Al in Al-doped HEAs will promote the formation of BCC/B2 phases [19, 20].

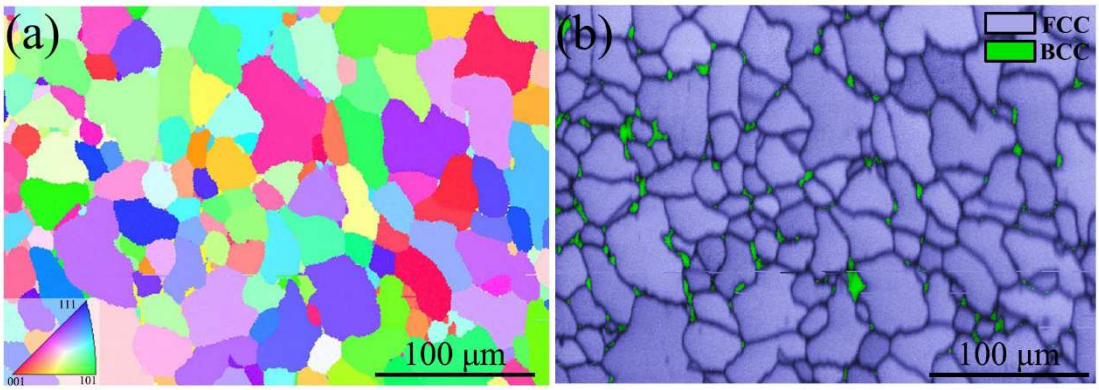

Fig. 3. EBSD analysis of the $Al_{13}Fe_{36}Co_{24}Ni_{24}C_3$ NS-MCA. (a) EBSD IPF map. (b) EBSD phase map corresponding to the EBSD IPF in (a).

For further characterizing the microstructure of the FCC grain interior, TEM and HRTEM were performed on the NS-MCA. The bright-field TEM image is presented in Figure 4(a), showing the nanostructured morphology obviously. It is evident that nano-sized particles with a high volume fraction of ~55 % are uniformly embedded in the matrix, coinciding with the result confirmed by the SEM image [Figure 2(b)]. The size distribution of the particles is exhibited in Figure 5, and the average diameter of these particles is 25 ± 2 nm. The inset of Figure 4(a) shows the representative corresponding SAED pattern with the zone axes of [011], indicating that the matrix has a FCC structure, whereas the additional faint superlattice diffraction spots (labeled by baby blue circles) reveal that these particles have an ordered-FCC ($L1_2$) structure. This feature will be further confirmed by the Fast Fourier Transformation (FFT) images [the right-hand site of Figure 4(b)] of the matrix and particles. Moreover, it is found that these $L1_2$ particles are interfacially coherent with the FCC matrix from the representative high-resolution TEM (HRTEM) image [Figure 4(b)], coupled with the FFT images. The lattice mismatch of the particle-matrix interface is determined to be ~ 0.28% for the NS-MCA. Moreover, the BCC grains [green regions in Figure 3(b)] present an ordered-BCC (B2) crystal structure, which can be demonstrated by the bright-field TEM image and corresponding SAED pattern of the BCC grain (Figure 6). Basing on these findings, hence, it can be concluded that our newly-developed alloy shows an interesting FCC + $L1_2$ dual-phase NS region and a small amount of B2 phases.

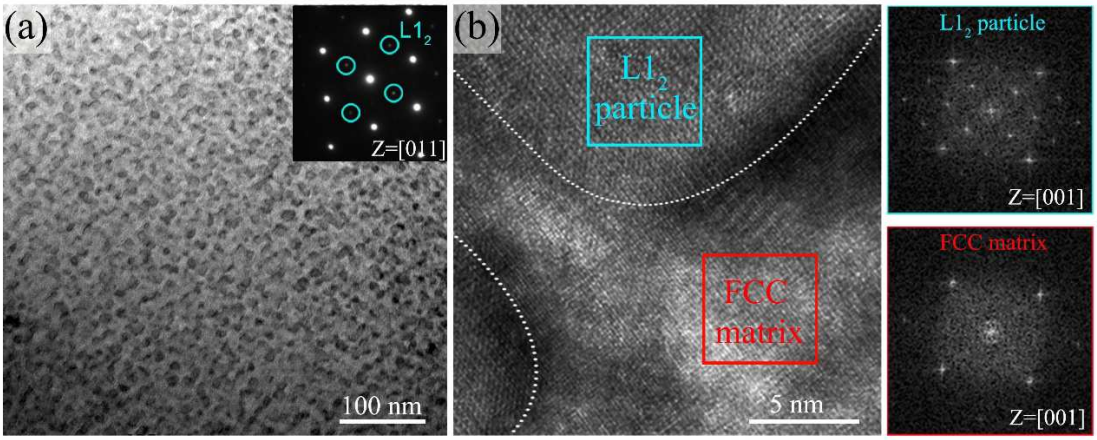

Fig. 4. TEM analysis of the $Al_{13}Fe_{36}Co_{24}Ni_{24}C_3$ NS-MCA. (a) TEM image of the NS-MCA, with the corresponding SAED pattern presented in the inset. (b) Representative HRTEM image showing the interface between the $L1_2$ particles and FCC matrix, with their corresponding FFT patterns on their right-hand side.

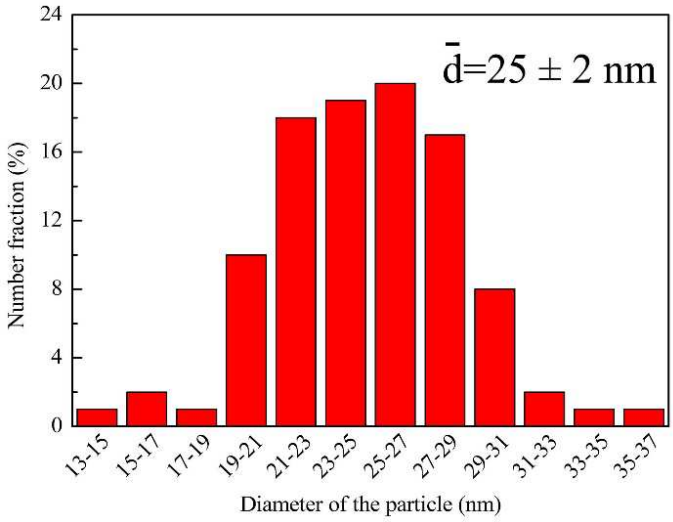

Fig. 5. The statistical particle diameter distribution in the NS region.

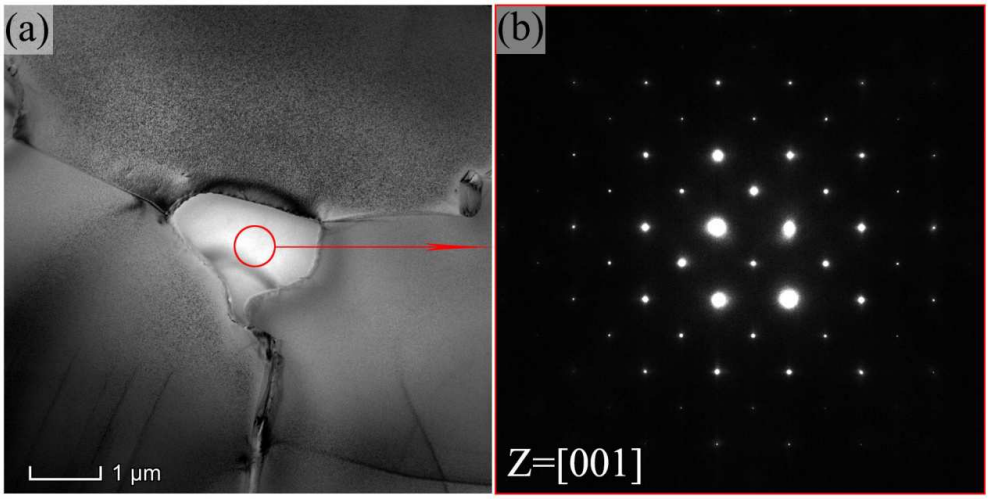

Fig. 6. TEM bright-field image (a) and corresponding selected-area electron diffraction (SAED) pattern (b) of the [001]-zone axis, showing a triple junction B2 phase.

The mechanical response of the NS-MCA is evaluated by compression tests at ambient temperature. Here we only focus on the true stresses and true strains, because they can provide more convictive description of materials deformation behaviors under compression tests. Figure 7 shows the representative true stress-strain curve in compression at the strain rate of 5×10^{-4} s^{-1}. The NS-MCA reveals the yield strength (σ_y) of ~ 1532 MPa, fracture strength (σ_f) of ~ 2365 MPa, and fracture strain (ε_f) of ~ 63%. To obtain an insight into the mechanical performance of the present NS-MCA, the compressive yield strength versus failure strain is plotted in Figure 8 alongside other previous reported nanostructured HEAs prepared by mechanical alloying ensued with spark plasma sintering (MA + SPS) [21-24], coarse-grained HEAs [25-28], and nanostructure-dendrite composite HEA [18] prepared directly by casting. It can be clearly observed that our newly-developed NS-MCA exhibits an exciting harmony of the compressive yield strength and fracture strain, making it have the potential application foreground in practice engineering applications.

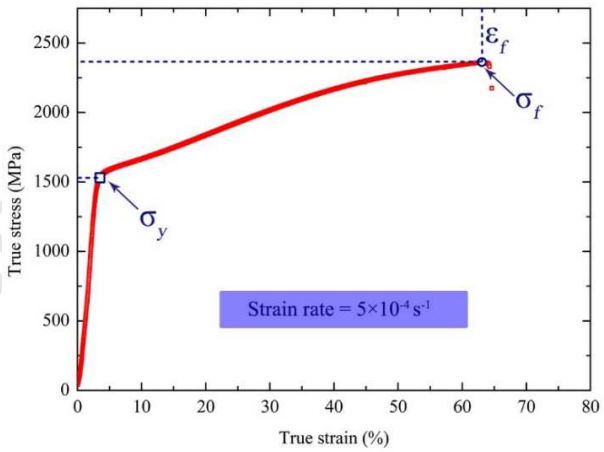

Fig. 7. Mechanical response of the $Al_{13}Fe_{36}Co_{24}Ni_{24}C_3$ NS-MCA. (a) Representative compressive true stress-strain plots. σ_y is the compressive yield strength(square), σ_f is the fracture strength (circle), and ε_f is the fracture strain.

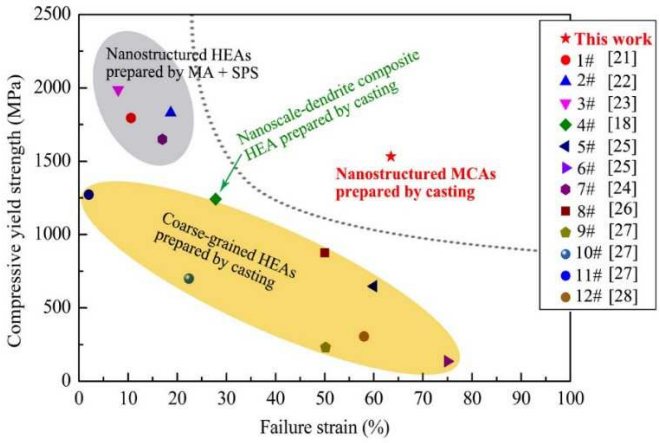

Fig. 8. Compressive yield strength versus failure strain of the present NS-MCA in comparison with previously-reported HEAs in literatures [18, 21-28]. Note that the 8# and 9# alloys were not failed during room-temperature compression tests.

We hypothesize that the high yield strength (~ 1.5 GPa) of the novel NS-MCA is primarily ascribed to the precipitation strengthening resulting from the high-density of the ordered $L1_2$ nanoparticles. Considering that the nanoparticles are coherent with the FCC matrix, and the $L1_2$ particles have an average diameter of ~ 25 nm, the dislocation shearing is generally thought to be the dominant mechanism [15, 29]. The increment of yielding strength induced by shearing strengthening, $\Delta\sigma_{sh}$, can be expressed as [30]:

$$\Delta\sigma_{sh} = 0.81M\frac{\gamma_{APB}}{2b}\left(\frac{3\pi f}{8}\right)^{\frac{1}{2}} \qquad (1)$$

where M = 3.06 for the FCC matrix (Taylor factor), f is the volume fraction (~0.55) of the $L1_2$ nanoparticles, b = ($\sqrt{2}$/2)·a = 0.2382 nm is the magnitude of the Burgers vector of the FCC matrix, with the lattice constant a = 0.3368 nm of the FCC matrix in the present work, and γ_{APB} is the anti-phase boundary (APB) free energy of the $L1_2$ nanoprecipitates. γ_{APB} = 184 mJ/m^2 is adopted from the corresponding binary $L1_2$ Ni_3Al precipitate [31]. Thus the value of $\Delta\sigma_{sh}$ can be calculated to be ~ 771 MPa using Equation (1). It is suggested that the shearing hardening from nanoprecipitates contributes to ~ 50% of the yield strength (~ 1532 MPa) of the NS-MCA. In addition to precipitate strengthening, contributions from the matrix, the grain-boundary strengthening and second phase (B2) strengthening may provide the remaining strength. In the present work, the grain-boundary strengthening is also assumed to critically conductive to the increment of the yield strength due to the fine-grain size of

the FCC (~ 33 μm) and B2 (~ 8.2 μm) phases. It is worth noting that the cooling rate from a water-cooled Cu-hearth is very fast and it plays a crucial role on the microstructure and mechanical properties of alloys. In order to facilitate this newly-developed alloy's promising and broad applications, our further studies are undergoing to investigate the effect of cooling rate on the microstructure and properties of the alloy.

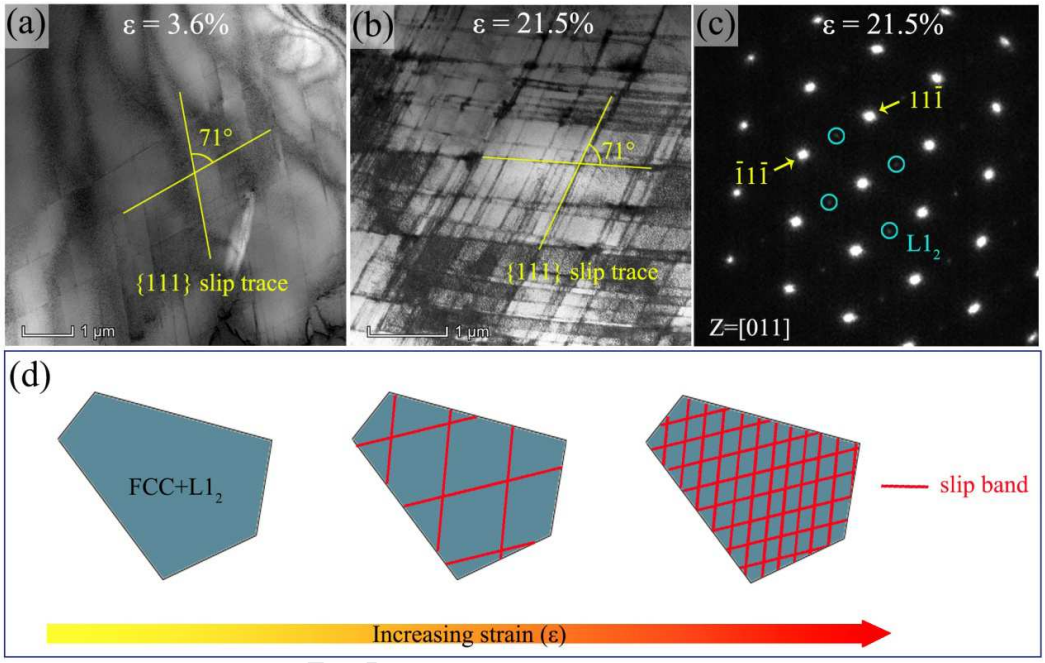

Fig. 9. TEM images showing the deformed microstructures of the FCC + $L1_2$ dual-phase NS region at different true strains: ε = 3.6% (a) and ε = 21.5% (b). (c) The corresponding SAED pattern along the [011] zone-axis of (b). (d) Schematic diagram depicting the dynamic slip band refinement in the NS region.

Finally, we carefully verified the underlying deformation mechanisms of our novel NS alloy with TEM (Figure 9 and Figure 10). Figures 9(a) and (b) present the representative in-grain deformation characteristics of the NS region of samples deformed to ~3.6% and ~21.5% true strains, respectively. At the true strain of ε = 3.6% [see Figure 9(a)], the dislocation structure is characterized by the multiple planar slip along the {111} primary slip planes, equal to that commonly observed in many FCC-type alloys [15, 32-34]. As the true compression strain increases to ~21.5% [Figure 9(b)], the microstructure of the NS region is also characterized by planar slip bands, as already discovered at ε = 3.6%. It is worth noting, however, that the slip band spacing is reduced, and the frequency of the intersecting slip bands is increased.

It can be confirmed that these planar dislocation slip along with the {111} slip planes [yellow solid lines in Figures 9(a) and (b)], combing with the corresponding SAED pattern along the [011] zone-axis of the deformed NS region at the true strain of ~ 21.5% [Figure 9(c)]. Gerold et al. [35] have already shown that the existence of the short-range order (SRO) as well as short range clustering (SRC) can promote the planar slip significantly. For this study, such slip planarity of dislocations should be related to the existence of $L1_2$ ordered nanoparticles. Unlike the NS region, the slip of screw dislocations is responsible for the deformation process in B2 grains (Figure 10). Similar observations have also been indicated in a B2-ordered $Al_{28}Co_{20}Cr_{11}Fe_{15}Ni_{26}$ high-entropy alloy [36].

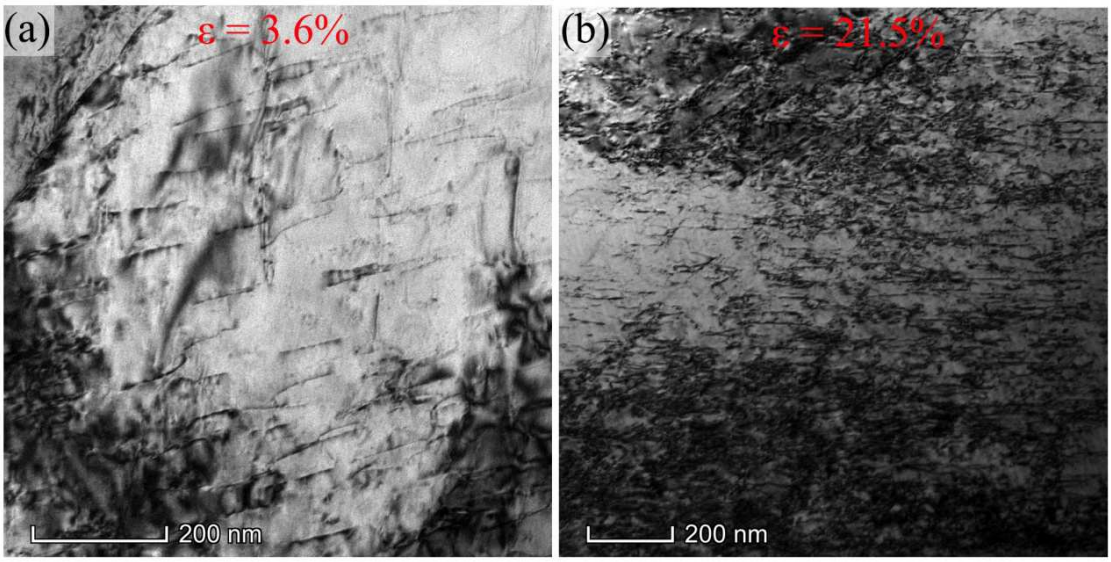

Fig. 10. Typical TEM micrographs of the B2 grain interior of samples deformed to 3.6% true strain (a) and 21.5% true strain (b).

The whole deformation microstructure evolution of the NS-MCA is thus characterized by the dramatically planar slip of dislocations in the NS region and screw dislocations glide in the B2 grain. For the NS region, with increasing the strain, the slip band substructure can be gradually refined. Figure 9(d) illustrates a schematic of the deformation-microstructure evolution of the NS region during straining. The dynamic slip band refinement in the NS regions can be evidently observed in Figure 9(d). During loading, such a dynamic refinement and/or intersection of the planar dislocation structure in fact is beneficial for the enhancement of strain hardening, and

thus conducive to postpone the onset of the plastic instability [37]. Moreover, the deformation substructure gives rise to the NS region subdivision and refinement, and then further helpful to the strength enhancement due to the dynamic Hall-Petch effect [15]. For the B2 grain, the slip of screw dislocations (Figure 10) suggests the B2 grain itself can also maintain a certain level of plastic deformation. By the comprehensive utilization of ductile NS regions and good deformability of B2 grains, the early cracking can be effectively suppressed, and eventually an outstanding combination of compression strength and plasticity can be obtained in the NS-MCA (Figures 7 and 8).

4. Conclusions

In summary, a new $Al_{13}Fe_{36}Co_{24}Ni_{24}C_3$ NS-MCA with an FCC + $L1_2$ dual-phase NS region and a small amount (~ 2.5 vol. %) of the B2 phase was successfully developed by suction casting directly. The newly-developed NS-MCA presents the compressive yield strength of ~1532 MPa, fracture strength of ~2365 MPa, and fracture strain of ~63%. As compared to the other previous reported HEAs/MCAs, the $Al_{13}Fe_{36}Co_{24}Ni_{24}C_3$ NS-MCA shows the outstanding combination of strength and plasticity. The deformation micro-mechanisms were systematically analyzed using transmission electron microscopy. Results show that the NS region and B2 grain are dominated by the pronounced planar slip and screw screw-dislocation slip, respectively. The good coordinate deformation between the FCC+$L1_2$ dual-phase NS region and B2 grains makes the newly-developed NS-MCA exhibit the outstanding combination of compression strength and plasticity.

Acknowledgements

The present work was financially supported by the National Science Foundation of China (Grant No. 11674274 and 51601166). P.K. Liaw very much appreciates the support of the U.S. Army Research Office project (W911NF-13-1-0438 and W911NF-19-2-0049) with the program managers, Drs. M. P. Bakas, S. N. Mathaudhu, and D. M. Stepp. PKL thanks the support from the National Science Foundation (DMR-1611180 and 1809640) with the program directors, Drs. G. Shiflet and D. Farkas.

References

[1] K.S. Kumar, S. Suresh, M.F. Chisholm, J.A. Horton, P. Wang, Deformation of electrodeposited nanocrystalline nickel, Acta Mater. 51(2) (2003) 387-405.

[2] S. Xue, Q. Li, D.Y. Xie, Y.F. Zhang, H. Wang, H.Y. Wang, J. Wang, X. Zhang, High strength, deformable nanotwinned Al–Co alloys, Mater. Res. Lett. 7(1) (2019) 33-39.

[3] K.C. Zuo, B. Blackman, J.G. Williams, H. Steininger, The Fracture and Fatigue Behaviour of Nano-Modified SAN, Adv. Mater. Res. 118-120 (2010) 43-48.

[4] A. Singh, L. Tang, M. Dao, L. Lu, S. Suresh, Fracture toughness and fatigue crack growth characteristics of nanotwinned copper, Acta Mater. 59(6) (2011) 2437-2446.

[5] M. George, Rigid biological systems as models for synthetic composites, Science. 310(5751) (2005) 1144-1147.

[6] J.W.C. Dunlop, P. Fratzl, Biological Composites, Annu. Rev. Mater. Res. 40(1) (2010) 1-24.

[7] W.S. Zhao, N.R. Tao, J.Y. Guo, Q.H. Lu, K. Lu, High density nano-scale twins in Cu induced by dynamic plastic deformation, Scr. Mater. 53(6) (2005) 745-749.

[8] P.V. Liddicoat, X.-Z. Liao, Y. Zhao, Y. Zhu, M.Y. Murashkin, E.J. Lavernia, R.Z. Valiev, S.P. Ringer, Nanostructural hierarchy increases the strength of aluminium alloys, Nat. Commun. 1(6) (2010) 1-7.

[9] Y. Lu, X. Gao, Y. Dong, T. Wang, H.-L. Chen, H. Maob, Y. Zhao, H. Jiang, Z. Cao, T. Li, S. Guo, Preparing bulk ultrafine-microstructure high-entropy alloys via direct solidification, Nanoscale. 10(4) (2018) 1912-1919.

[10] S.-K.C. Jien-Wei Yeh, Su-Jien Lin, Jon-Yiew Gan, Nanostructured High-Entropy Alloys with Multiple Principle Elements: Novel Alloy Design Concepts Outcomes**, Adv. Eng. Mater. 6(5) (2004) 299–303.

[11] B. Cantor, I.T.H. Chang, P. Knight, A.J.B. Vincent, Microstructural development in equiatomic multicomponent alloys, Mater. Sci. Eng. A. 375–377 (2004) 213-218.

[12] M. Komarasamy, T. Wang, K. Liu, R.S. Mishra, Hierarchical multi-phase microstructural architecture for exceptional strength-ductility combination in a complex concentrated alloy via high-temperature severe plastic deformation, Scr.

Mater. 162 (2019) 38-43.

[13] Y. Lu, Y. Dong, S. Guo, L. Jiang, H. Kang, T. Wang, B. Wen, Z. Wang, J. Jie, Z. Cao, H. Ruan, T. Li, A Promising New Class of High-Temperature Alloys: Eutectic High-Entropy Alloys, Sci. Rep. 4 (2014) 6200.

[14] Z. Lei, X. Liu, Y. Wu, H. Wang, S. Jiang, S. Wang, X. Hui, Y. Wu, B. Gault, P. Kontis, D. Raabe, L. Gu, Q. Zhang, H. Chen, H. Wang, J. Liu, K. An, Q. Zeng, T.-G. Nieh, Z. Lu, Enhanced strength and ductility in a high-entropy alloy via ordered oxygen complexes, Nature. 563 (2018) 546-550.

[15] T. Yang, Y.L. Zhao, Y. Tong, Z.B. Jiao, J. Wei, J.X. Cai, X.D. Han, D. Chen, A. Hu, J.J. Kai, K. Lu, Y. Liu, C.T. Liu, Multicomponent intermetallic nanoparticles and superb mechanical behaviors of complex alloys, Science. 362(6417) (2018) 933.

[16] B. Gludovatz, A. Hohenwarter, D. Catoor, E.H. Chang, E.P. George, R.O. Ritchie, Science. 345(6201) (2014) 153-1158.

[17] Y. Zhang, T.T. Zuo, Z. Tang, M.C. Gao, K.A. Dahmen, P.K. Liaw, Z.P. Lu, Microstructures and properties of high-entropy alloys, Prog. Mater. Sci. 61 (2014) 1-93.

[18] J.T. Fan, L.J. Zhang, P.F. Yu, M.D. Zhang, G. Li, P.K. Liaw, R.P. Liu, A novel high-entropy alloy with a dendrite-composite microstructure and remarkable compression performance, Scr. Mater. 159 (2019) 18-23.

[19] X. Sun, H. Zhang, S. Lu, X. Ding, Y. Wang, L. Vitos, Phase selection rule for Al-doped CrMnFeCoNi high-entropy alloys from first-principles, Acta. Mater. 140 (2017) 366-374.

[20] J.Y. He, W.H. Liu, H. Wang, Y. Wu, X.J. Liu, T.G. Nieh, Z.P. Lu, Effects of Al addition on structural evolution and tensile properties of the FeCoNiCrMn high-entropy alloy system, Acta. Mater. 62 (2014) 105-113.

[21] Z. Fu, W. Chen, H. Wen, D. Zhang, Z. Chen, B. Zheng, Y. Zhou, E.J. Lavernia, Microstructure and strengthening mechanisms in an FCC structured single-phase nanocrystalline Co25Ni25Fe25Al7.5Cu17.5 high-entropy alloy, Acta. Mater. 107 (2016) 59-71.

[22] Z. Fu, B.E. MacDonald, D. Zhang, B. Wu, W. Chen, J. Ivanisenko, H. Hahn, E.J.

Lavernia, Fcc nanostructured TiFeCoNi alloy with multi-scale grains and enhanced plasticity, Scr. Mater. 143 (2018) 108-112.

[23] W. Ji, W. Wang, H. Wang, J. Zhang, Y. Wang, F. Zhang, Z. Fu, Alloying behavior and novel properties of CoCrFeNiMn high-entropy alloy fabricated by mechanical alloying and spark plasma sintering, Intermetallics. 56 (2015) 24-27.

[24] Y. Yin, J. Zhang, Q. Tan, W. Zhuang, N. Mo, M. Bermingham, M.-X. Zhang, Novel cost-effective Fe-based high entropy alloys with balanced strength and ductility, Mater. Des. 162 (2019) 24-33.

[25] T.-T. Shun, L.-Y. Chang, M.-H. Shiu, Microstructures and mechanical properties of multiprincipal component CoCrFeNiTi$_x$ alloys, Mater. Sci. Eng. A. 556 (2012) 170-174.

[26] O.N. Senkov, J.M. Scott, S.V. Senkova, D.B. Miracle, C.F. Woodward, Microstructure and room temperature properties of a high-entropy TaNbHfZrTi alloy, J. Alloys Compd. 509(20) (2011) 6043-6048.

[27] X.F. Wang, Y. Zhang, Y. Qiao, G.L. Chen, Novel microstructure and properties of multicomponent CoCrCuFeNiTi$_x$ alloys, Intermetallics. 15(3) (2007) 357-362.

[28] T.-T. Shun, L.-Y. Chang, M.-H. Shiu, Microstructure and mechanical properties of multiprincipal component CoCrFeNiMo$_x$ alloys, Mater. Charact. 70 (2012) 63-67.

[29] Qing Wang, Yue Ma, Beibei Jiang, Xiaona Li, Yao Shi, Chuang Dong, Prter K. Liaw, A cuboidal B2 nanoprecipitation-enhanced body-centered-cubic alloy $Al_{0.7}CoCrFe_2Ni$ with prominent tensile properties, Scr. Mater. 120 (2016) 85-89.

[30] Nhon Q. Vo, Christian H. Liebscher, Michael J.S. Rawlings, Mark Asta, David C. Dunand, Creep properties and microstructure of a precipitation-strengthened ferritic Fe–Al–Ni–Cr alloy, Acta. Mater. 71 (2014) 89-99.

[31] T. Kruml, E. Conforto, B. Lo Piccolo, D. Caillard, J.L. Martin, From dislocation cores to strength and work-hardening: a study of binary NiAl, Acta. Mater. 50 (2002) 5091-5101.

[32] E. Welsch, D. Ponge, S.M. Hafez Haghighat, S. Sandlöbes, P. Choi, M. Herbig, S. Zaefferer, D. Raabe, Strain hardening by dynamic slip band refinement in a high-Mn lightweight steel, Acta. Mater. 116 (2016) 188-199.

[33] B. Uzer, S. Picak, J. Liu, T. Jozaghi, D. Canadinc, I. Karaman, Y.I. Chumlyakov, I. Kireeva, On the mechanical response and microstructure evolution of NiCoCr single crystalline medium entropy alloys, Mater. Res. Lett. 6(8) (2018) 442-449.

[34] B. Ma, C. Li, J. Zheng, Y. Han, Strain hardening behavior and deformation substructure of Fe–20/27Mn–4Al–0.3C non-magnetic steels, Mater. Des. 92 (2016) 313-321.

[35] V. Gerold, H.P. Karnthaler, On the origin of planar slip in f.c.c. alloys, Acta. Metal. 37(8) (1989) 2177-2183.

[36] M. Feuerbacher, Dislocations and deformation microstructure in a B2-ordered Al28Co20Cr11Fe15Ni26 high-entropy alloy, Sci. Rep. 6 (2016) 29700.

[37] Y.L. Zhao, T. Yang, J.H. Zhu, D. Chen, Y. Yang, A. Hu, C.T. Liu, J.J. Kai, Development of high-strength Co-free high-entropy alloys hardened by nanosized precipitates, Scr. Mater. 148 (2018) 51–55.

Figures caption

Fig. 1. XRD scattering and SEM/EBSD analysis of the $Al_{13}Fe_{36}Co_{24}Ni_{24}C_3$ NS-MCA.
Fig. 2. The BSE-SEM image of the $Al_{13}Fe_{36}Co_{24}Ni_{24}C_3$ NS-MCA. (b) High magnification SEM image of the interior of the FCC grains, showing the nanostructured morphology.
Fig. 3. EBSD analysis of the $Al_{13}Fe_{36}Co_{24}Ni_{24}C_3$ NS-MCA. (a) EBSD IPF map. (b) EBSD phase map corresponding to the EBSD IPF in (a).
Fig. 4. TEM analysis of the $Al_{13}Fe_{36}Co_{24}Ni_{24}C_3$ NS-MCA. (a) TEM image of the NS-MCA, with the corresponding SAED pattern presented in the inset. (b) Representative HRTEM image showing the interface between the $L1_2$ particles and FCC matrix, with their corresponding FFT patterns on their right-hand side.
Fig. 5. The statistical particle diameter distribution in the NS region.
Fig. 6. TEM bright-field image (a) and corresponding selected-area electron diffraction (SAED) pattern (b) of the [001]-zone axis, showing a triple junction B2 phase.
Fig. 7. Mechanical response of the $Al_{13}Fe_{36}Co_{24}Ni_{24}C_3$ NS-MCA. (a) Representative compressive true stress-strain plots. σ_y is the compressive yield strength(square), σ_f is the fracture strength (circle), and ε_f is the fracture strain.
Fig. 8. Compressive yield strength versus failure strain of the present NS-MCA in comparison with previously-reported HEAs in literatures [18, 21-28]. Note that the 8# and 9# alloys were not failed during room-temperature compression tests.
Fig. 9. TEM images showing the deformed microstructures of the FCC + $L1_2$ dual-phase NS region at different true strains: ε = 3.6% (a) and ε = 21.5% (b). (c) The corresponding SAED pattern along the [011] zone-axis of (b). (d) Schematic diagram depicting the dynamic slip band refinement in the NS region.
Fig. 10. Typical TEM micrographs of the B2 grain interior of samples deformed to 3.6% true strain (a) and 21.5% true strain (b).

Declaration of interests

☒ The authors declare that they have no known competing financial interests or personal relationships that could have appeared to influence the work reported in this paper.

☐The authors declare the following financial interests/personal relationships which may be considered as potential competing interests: